Experimental Verification of Intrinsic Pressure Framework in an Activity Landscape

Zihao Sun(孙子豪)[1,2†], Longfei Li(黎龙飞)[1†], Chuyun Wang(汪楚云)[3†], Jing Wang(王璟)[4], Huaicheng Chen(陈怀城)[4], Gao Wang(王高)[4], Fangfu Ye(叶方富)[1,2,4,5*], Liyu Liu(刘雳宇)[6,4*], and Mingcheng Yang(杨明成)[1,2*]

[1]*Beijing National Laboratory for Condensed Matter Physics and Laboratory of Soft Matter Physics, Institute of Physics, Chinese Academy of Sciences, Beijing 100190, China*
[2]*School of Physical Sciences, University of Chinese Academy of Sciences, Beijing 100049, China*
[3]*Postgraduate Training Base Alliance, Wenzhou Medical University, Wenzhou 325035, China*
[4]*Wenzhou Institute, University of Chinese Academy of Sciences, Wenzhou 325001, China*
[5]*Oujiang Laboratory (Zhejiang Lab for Regenerative Medicine, Vision and Brain Health), Wenzhou 325000, China*
[6]*Human Phenome Institute, Fudan University, Shanghai 201203, China*

(Received 5 November 2025; accepted manuscript online 26 November 2025)

The intrinsic pressure framework, which treats self-propelling force as an external force, provides a convenient and consistent description of mechanical equilibrium in active matter. However, direct experimental evidence is still lacking. To validate this framework, here we employ a programmable robotic platform, where a single light-controlled wheeled robot travels in an activity landscape. Our experiments quantitatively demonstrate that the intrinsic pressure difference across the activity interface is balanced by the emerged polarization force. This result unambiguously confirms the theoretical predictions, thus validating the intrinsic pressure framework and laying the experimental foundation for the intrinsic pressure-based mechanical description of dry active matter.

DOI: 10.1088/0256-307X/43/1/010901 CSTR: 32039.14.0256-307X.43.1.010901

1. Introduction. Active matter systems comprise self-propelled units that continuously dissipate energy, ranging from flocking birds to synthetic microswimmers.[1–3] These systems often exhibit self-organization patterns like motility-induced phase separation (MIPS)[4–8] and large-scale collective motions,[9–15] which challenge conventional equilibrium intuition. These nonequilibrium phenomena have stimulated intense investigation into the fundamental physics of active systems.[1,2,16–18] An important issue in this field is the ongoing debate over the definition of pressure and its role in establishing mechanical equilibrium, particularly in complex active systems.

The core of this debate stems from different mechanical treatments of self-propelling force. The dominant active pressure (P^{a}) framework incorporates the self-propulsion contribution into the stress tensor and has successfully explained diverse phenomena such as phase behavior and forces on immersed objects.[19–22] This framework works quite well for minimal torque-free active particles with uniform activity, for which P^{a} is known to be a state function,[20,23] as also supported by experiments of dilute active colloids.[24–27] In more generic active systems involving torques, inhomogeneous activity or communicating couplings, however, P^{a} is not a well-defined state function.[23,28–31] Furthermore, the establishment of mechanical equilibrium necessitates introducing complex auxiliary terms that lack a clear mechanical interpretation,[29,32,33] and even the local definition of P^{a} becomes ambiguous. These complications not only obscure the intuitive physical understanding of P^{a}-based mechanical equilibrium but also limit its universal applicability. In contrast, the intrinsic pressure (P^{i}) framework treats self-propulsion as an effective external force, identifying pressure solely through kinetic and interaction contributions analogous to conventional passive systems.[34–36] This framework is convenient and universal for generic active systems, maintaining local pressure as a well-defined state function and naturally restoring straightforward mechanical equilibrium without invoking auxiliary terms. Though its broad validity has been confirmed by extensive simulations,[33] the P^{i} framework currently lacks direct experimental verification.

To bridge this gap, we develop a macroscopic active matter platform to directly test the P^{i}-based mechanical equilibrium, where a light-controlled wheeled robot (MARK II) moves in an activity landscape. We first outline the theoretical framework based on the intrinsic pressure, then describe the experimental setup designed to validate this framework. Our experiments enable measurement of the pressure profile and polarization force density, demonstrating that the pressure difference is balanced by the emerged polarization force near the activity interface. This provides a quantitative experimental verification of the P^{i} framework for the first time, thereby highlighting

†These authors contributed equally to this work.
*Corresponding authors. Email: fye@iphy.ac.cn; lyliu@cqu.edu.cn; mcyang@iphy.ac.cn

its validity in dry active matter. Furthermore, the presented platform establishes a novel approach for quantitative tests of mechanical behavior of diverse active systems.

2. Theory. We consider a generic model of underdamped active particles in two dimensions. Each particle i, with mass M_0 and rotational inertia I, is driven by a self-propelling force $\boldsymbol{F}_i^{\mathrm{a}} = \gamma_{\mathrm{t}} v_0 \boldsymbol{e}_i$, where $\boldsymbol{e}_i = (\cos\theta_i, \sin\theta_i)$. The motion of particle i is generally governed by the following Langevin equations:

$$\begin{aligned} M_0 \frac{\mathrm{d}\boldsymbol{v}_i}{\mathrm{d}t} &= -\gamma_{\mathrm{t}}(\boldsymbol{v}_i - v_0 \boldsymbol{e}_i) + \sum_{j\neq i} \boldsymbol{F}_{ij}^{\mathrm{int}} + \boldsymbol{F}_i^{\mathrm{ext}} + \sqrt{2\gamma_{\mathrm{t}} k_{\mathrm{B}} T}\, \boldsymbol{\eta}_i, \\ I \frac{\mathrm{d}\omega_i}{\mathrm{d}t} &= -\gamma_{\mathrm{r}}(\omega_i - \omega_0) + \sum_{j\neq i} \Gamma_{ij}^{\mathrm{int}} + \Gamma_i^{\mathrm{ext}} + \sqrt{2\gamma_{\mathrm{r}} k_{\mathrm{B}} T}\, \xi_i, \end{aligned} \quad (1)$$

where γ_{t} and γ_{r} are the translational and rotational friction coefficients; v_0 and ω_0 denote the self-propelling and self-rotating speeds; $\boldsymbol{F}_{ij}^{\mathrm{int}}$ and $\Gamma_{ij}^{\mathrm{int}}$ represent interparticle forces and torques; and $\boldsymbol{F}_i^{\mathrm{ext}}$ and Γ_i^{ext} account for external forces and torques. The stochastic translational noise $\boldsymbol{\eta}_i$ and rotational noise ξ_i are Gaussian white noise with zero means and correlations $\langle \boldsymbol{\eta}_i(t)\boldsymbol{\eta}_j(t')\rangle = \mathbf{I}\delta_{ij}\delta(t-t')$, $\langle \xi_i(t)\xi_j(t')\rangle = \delta_{ij}\delta(t-t')$.

The noise-averaged probability distribution function is defined as $\psi(\boldsymbol{r},\boldsymbol{v},\theta,\omega,t) = \langle\hat{\psi}(\boldsymbol{r},\boldsymbol{v},\theta,\omega,t)\rangle$, with $\hat{\psi} = \sum_i \delta[\boldsymbol{r}-\boldsymbol{r}_i(t)]\delta[\boldsymbol{v}-\boldsymbol{v}_i(t)]\delta[\theta-\theta_i(t)]\delta[\omega-\omega_i(t)]$. The corresponding Fokker–Planck equation reads [37]

$$\begin{aligned} \frac{\partial\psi}{\partial t} &= -\nabla\cdot[\boldsymbol{v}\psi] - \frac{\partial}{\partial\theta}[\omega\psi] + \frac{\gamma_{\mathrm{t}} k_{\mathrm{B}} T}{M_0^2}\nabla_{\boldsymbol{v}}^2\psi + \frac{\gamma_{\mathrm{r}} k_{\mathrm{B}} T}{I^2}\frac{\partial^2\psi}{\partial\omega^2} \\ &- \frac{1}{M_0}\nabla_{\boldsymbol{v}}\cdot\Big[-\gamma_{\mathrm{t}}(\boldsymbol{v}-v_0\boldsymbol{e})\psi + \int \mathrm{d}\Omega' \boldsymbol{F}^{\mathrm{int}}\langle\hat{\psi}'\hat{\psi}\rangle + \boldsymbol{F}^{\mathrm{ext}}\psi\Big] \\ &- \frac{1}{I}\frac{\partial}{\partial\omega}\Big[-\gamma_{\mathrm{r}}(\omega-\omega_0)\psi + \int \mathrm{d}\Omega' \Gamma^{\mathrm{int}}\langle\hat{\psi}'\hat{\psi}\rangle + \Gamma^{\mathrm{ext}}\psi\Big], \end{aligned} \quad (2)$$

where $\mathrm{d}\Omega' = \mathrm{d}\boldsymbol{r}'\mathrm{d}\boldsymbol{v}'\mathrm{d}\theta'\mathrm{d}\omega'$ denotes the phase space volume element for notational simplicity.

Without loss of generality, the system is assumed to be translationally invariant along the y direction. In the steady state ($\partial_t\psi = 0$), multiplying Eq. (2) by $\boldsymbol{v}$ and integrating over $\boldsymbol{v}$, θ ,and ω yields the particle flux along x,

$$\gamma_{\mathrm{t}} J_x^{\mathrm{n}} = f_x^{\mathrm{m}} + f_x^{\mathrm{ext}} - \frac{\mathrm{d}P^{\mathrm{k}}}{\mathrm{d}x} + I_1(x), \quad (3)$$

where the particle flux (J_x^{n}), polarization force density (f_x^{m}), external force density (f_x^{ext}), kinetic pressure (P^{k}), and interaction term [$I_1(x)$] are separately defined as

$$\begin{aligned} n &\equiv \int \mathrm{d}\boldsymbol{v}\int \mathrm{d}\theta \int \mathrm{d}\omega\ \psi, \\ J_x^{\mathrm{n}} &\equiv n\langle v_x\rangle = \int \mathrm{d}\boldsymbol{v} v_x \int \mathrm{d}\theta \int \mathrm{d}\omega\ \psi, \\ f_x^{\mathrm{m}} &\equiv n\langle\gamma_{\mathrm{t}} v_0\cos\theta\rangle = \int \mathrm{d}\boldsymbol{v}\int \mathrm{d}\theta\cos\theta\int \mathrm{d}\omega\ \gamma_{\mathrm{t}} v_0\psi, \\ f_x^{\mathrm{ext}} &\equiv n\langle F^{\mathrm{ext}}\rangle = \int \mathrm{d}\boldsymbol{v}\int \mathrm{d}\theta\int \mathrm{d}\omega\ F_x^{\mathrm{ext}}\psi, \\ P^{\mathrm{k}} &\equiv nM_0\langle v_x^2\rangle = \int \mathrm{d}\boldsymbol{v}\ v_x^2\int \mathrm{d}\theta\int \mathrm{d}\omega\ \psi, \\ I_1(x) &\equiv \int \mathrm{d}\boldsymbol{v}\int \mathrm{d}\theta\int \mathrm{d}\omega\int \mathrm{d}\Omega' F_x^{\mathrm{int}}\langle\hat{\psi}'\hat{\psi}\rangle. \end{aligned} \quad (4)$$

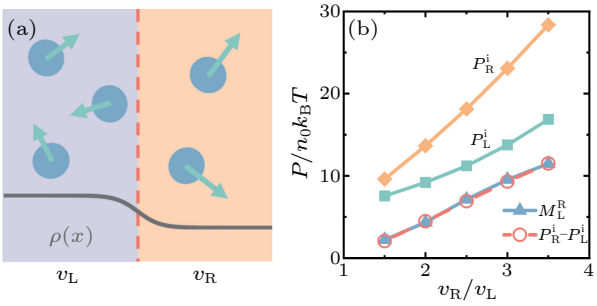

Fig. 1. (a) Sketch of an active system with a piecewise activity, where the propulsion speed of a particle is v_{L} in the left region and v_{R} in the right region. (b) The bulk pressures, the pressure difference, and the integral of polarization force density as functions of speed ratio $v_{\mathrm{R}}/v_{\mathrm{L}}$ for ideal underdamped active particles, with $n_0 = 1.0$, $M_0 = 10$, $I = 0.1$, $\gamma_{\mathrm{t}} = \gamma_{\mathrm{r}} = 1$, $\omega_0 = 0$, and $v_{\mathrm{L}} = 1.0$.

Notably, $I_1(x)$ relates to the interaction pressure by $P^{\mathrm{c}}(x) = \int_x^\infty I_1(x')\mathrm{d}x'$. [20,32,34] Thus, equation (3) exactly corresponds to local force balance,

$$\frac{\mathrm{d}P^{\mathrm{i}}}{\mathrm{d}x} = f_x^{\mathrm{m}} + f_x^{\mathrm{ext}} - \gamma_{\mathrm{t}} J_x^{\mathrm{n}}, \quad (5)$$

where the intrinsic pressure $P^{\mathrm{i}} = P^{\mathrm{k}} + P^{\mathrm{c}}$ includes kinetic and interaction contributions. Note that the polarization force emerged from the self-propelling force is treated as an external force from the substrate.

Consider a system with a piecewise activity pattern, where the self-propelling velocity of particles is set to v_{L} in the left region and v_{R} in the right region, as sketched in Fig. 1(a). For a flux-free steady state ($J_x^{\mathrm{n}} = 0$) without external field, integrating Eq. (5) yields

$$P_{\mathrm{R}}^{\mathrm{i}} - P_{\mathrm{L}}^{\mathrm{i}} = \int_{\mathrm{L}}^{\mathrm{R}} f_x^{\mathrm{m}}\mathrm{d}x = M_{\mathrm{L}}^{\mathrm{R}}, \quad (6)$$

where L and R are taken deep into the corresponding bulk phases. Equation (6) indicates that activity differences induce polarization force near the activity interfaces between the two regions, compensating intrinsic pressure disparities. In systems without interparticle interactions, P^{c} vanishes and thus the intrinsic pressure reduces to $P^{\mathrm{i}} = P^{\mathrm{k}}$.

Before conducting experimental verification, we simulate non-interacting underdamped active particles in the activity landscape described above. By varying the velocity ratio $v_{\mathrm{R}}/v_{\mathrm{L}}$, the intrinsic pressures and polarization force are determined and Eq. (6) is quantitatively verified as shown in Fig. 1. With the framework validated in this idealized model, we now proceed to test its robustness in a real physical system, as detailed in the following sections.

3. Experiment Setup. The experimental system, illustrated in Fig. 2(a), is designed to realize and study underdamped active dynamics in a controlled activity landscape. This system comprises three core components: the MARK II light-controlled robots, a bottom LED platform, and an overhead camera. This integrated setup enables real-time modulation of robotic motion states through dynamic adjustment of regional brightness, creating spatially non-uniform activity patterns.

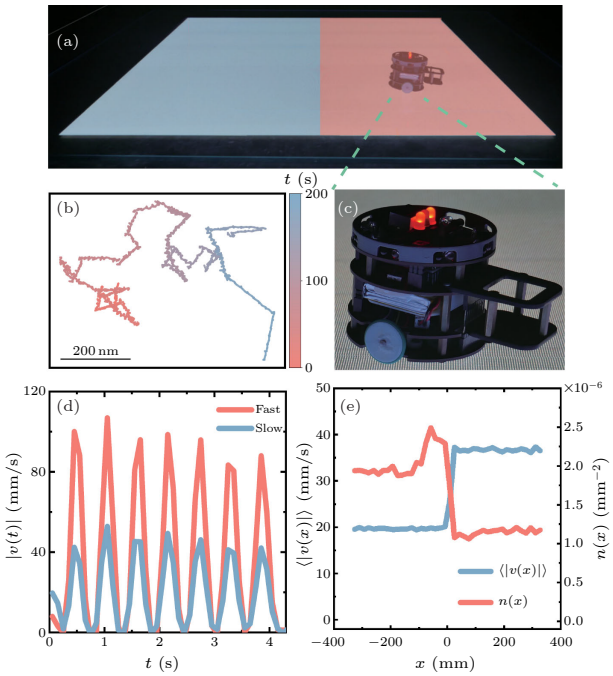

Fig. 2. (a) Experimental schematic depicting a controllable robot randomly traveling between low-activity (left, blue) and high-activity (right, red) regions with an interface at $x = 0$. The robot reverses the direction of self-propulsion upon contacting the forbidden region (black area) boundaries. (b) A representative trajectory schematic of the robot's motion within the experimental area. The color gradient from red to blue indicates the progression of time. (c) The enlarged MARK II light-controlled programmable robot used in the experiment. (d) Instantaneous speed profile of the robot during a single linear advance, obtained by averaging trajectories within the corresponding low-activity (slow) and high-activity (fast) regions. (e) Average speed profile $\langle|v(x)|\rangle$ (blue curve) and position probability distribution $n(x)$ (red curve) along the x direction for a single robot, illustrating the inverse relationship between density and speed across the interface.

To avoid complex inter-robot interactions, a single MARK II robot [shown in Fig. 2(c)] is employed, functioning as an underdamped active particle with a mass of $M_0 = 234.85\,\mathrm{g}$. The two-wheeled robot features four TCS3200 color sensors arranged symmetrically on its bottom for real-time light sensing, along with a counterweight to maintain attitude stability during motion. An embedded computing unit processes light intensity measurements using a preset control algorithm to determine motion behaviors. Hall encoders provide velocity feedback, while pulse-width modulation corrects inter-wheel speed discrepancies to ensure stable locomotion. Three LED indicators on the top surface facilitate camera-based tracking of position and motion states.

The robot operates on a $1.2\,\mathrm{m} \times 1.2\,\mathrm{m}$ horizontal LED screen with RGB LEDs spaced at 1.25 mm intervals. The platform generates dynamically adjustable light fields within a central experimental area, while surrounding regions are designated as forbidden zones. The experimental area is partitioned into high-activity and low-activity zones by an interface at $x = 0$. For real-time control, an overhead camera captures images at 0.08 s intervals to track the robot's position [a representative trajectory is shown in Fig. 2(b)], and a computer processes these data to dynamically adjust LED light intensity based on the robot's zone location.

Within this programmable environment, the MARK II robot moves in the experimental area with four distinct motion states: high-speed linear motion, low-speed linear motion, random rotation, and obstacle avoidance. Prior to initiating linear motion, the number of advancement steps (4–7) is determined by a uniformly distributed random number generator. Each step consists of alternating 0.3 s powered and unpowered intervals, producing the oscillatory speed profile shown in Fig. 2(d). During these unpowered intervals, the robot senses environmental light intensity to inform subsequent behavioral decisions, such as obstacle avoidance or speed adjustment. After completing linear motion, the robot enters a random rotation state, turning its self-propelling orientation by a uniformly distributed angle $\theta \in [0, 2\pi]$. If any color sensor detects zero light intensity (indicating entry into the forbidden region), the robot immediately switches to obstacle avoidance mode and reverses direction into the experimental area.

This programmable, closed-loop platform enables the investigation of mechanical equilibrium in spatially inhomogeneous activity patterns, as demonstrated in the following section.

4. Experimental Verification. The experimental setup provides a controlled environment to study the behavior of the MARK II robot moving in an activity landscape. Over 55 hours of experiments, we tracked the robot's motion trajectory. As shown in Fig. 2(e), when the robot crosses the interface from high- to low-activity zones, its average speed decreases from 36.74 mm/s to 19.69 mm/s. The observed density distribution shows that the robot spends more time in the low-activity region, consistent with the expected inverse relationship between probability density and propulsion speed in the bulk phases.[8,38,39]

In this single-robot system, the pressure originates solely from the robot's motion: $P^{\mathrm{i}} = P^{\mathrm{k}} = nM_0\langle v_x^2\rangle$. Given the roughly inverse relation between density and speed, a pressure difference between the low-activity and high-activity regions arises, which should be balanced by the polarization forces near the interface. Testing this mechanical equilibrium requires accurate measurement of both the kinetic pressure and the polarization force density from the robot's trajectory data.

A central challenge for calculating the polarization force density is that the self-propelling force $\boldsymbol{F}^{\mathrm{a}}$ cannot be measured directly. Nevertheless, this force can be inferred from Newton's second law,

$$\boldsymbol{F}^{\mathrm{a}} = M_0\boldsymbol{a} + F^{\mathrm{f}}\hat{\boldsymbol{v}}, \tag{7}$$

where $\boldsymbol{a}$ is the robot's acceleration, $\hat{\boldsymbol{v}}$ is the orientation of velocity and F^{f} is the friction from the substrate. Accurate determination of $\boldsymbol{F}^{\mathrm{a}}$ therefore requires independent characterization of the friction F^{f}.

We measured the friction force by dragging an unpowered robot at constant speeds (Fig. 3). The gears connecting the motor to the wheels were removed to ensure

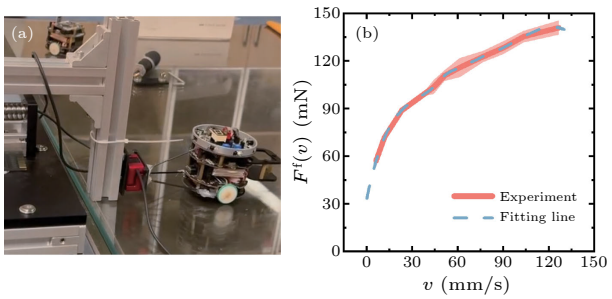

Fig. 3. (a) Experimental setup for friction measurement: a linear slide with a force sensor pulls the unpowered robot at controlled speeds. (b) Measured friction force (red solid line) and the fitting curve $F^{\rm f}(v)$ (blue dashed line) used for subsequent analysis.

that only wheel-substrate friction was measured, and the connection structure kept the robot's attitude during active motion. The measured pulling force versus velocity is interpolated to obtain $F^{\rm f}(v)$ for subsequent analysis [see Fig. 3(b)].

With the friction determined, we proceed to analyze the experimental trajectories. We extracted the instantaneous velocity $\boldsymbol{v}$ and acceleration $\boldsymbol{a}$ from the trajectory data during linear motion, excluding intervals of random rotation during which the speed drops to nearly zero. This isolation of linear motion allows for a one-dimensional treatment, as the dynamics during each propulsive segment are effectively confined to a single direction ($\hat{\boldsymbol{v}} = \boldsymbol{e}$). From this processed data, we obtained the polarization force density $f_x^{\rm m} = n\langle F_x^{\rm a}\rangle$ and kinetic pressure $M_0 n\langle v_x^2\rangle$, as plotted in Fig. 4(a). Note that we excluded the trajectory data within 200 mm of the forbidden region edges, a distance greater than the robot's persistence length ($l \approx 150$ mm), to avoid boundary effects.

The $P^{\rm i}$-based mechanical equilibrium is tested in Fig. 4(b), which compares the pressure difference $P_{\rm R}^{\rm i} - P_{\rm L}^{\rm i}$ with the integrated polarization force $M_{\rm L}^{\rm R} = \int_{\rm L}^{\rm R} f_x^{\rm m}{\rm d}x$ across the interface. The measured values are in good agreement:

$$\begin{aligned} P_{\rm R}^{\rm i} - P_{\rm L}^{\rm i} &\approx 1.50 \times 10^{-4}\,{\rm mN/mm}, \\ \overline{M_{\rm L}^{\rm R}} &\approx 1.55 \times 10^{-4}\,{\rm mN/mm}, \end{aligned} \tag{8}$$

where $\overline{M_{\rm L}^{\rm R}}$ denotes the average of integrated polarization force. The close agreement between the measured pressure difference and the integrated polarization force provides direct experimental validation for the intrinsic pressure framework in an underdamped active system.

Finally, it should be pointed out that Söker *et al.*[40] investigated polarization at activity interfaces in a dilute active colloidal system and tried to link it to the active pressure concept; however, they did not explicitly examine force balance across the interface. Indeed, an analysis of their results indicates that mechanical equilibrium cannot be established within the $P^{\rm a}$ framework without including auxiliary terms.

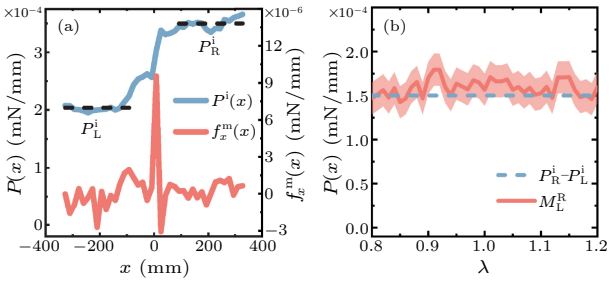

Fig. 4. (a) Intrinsic pressure $P^{\rm i}$ (blue curve) and polarization force density $f_x^{\rm m}$ (red curve) versus x-position, which are calculated according to Eq. (4). Dashed black lines denote bulk-phase pressures. Near the activity interface ($x = 0$), the polarization force predominantly in the $+x$-direction counterbalances the intrinsic pressure difference. (b) Integrated polarization force density $M_{\rm L}^{\rm R}$ (solid red line, shading: 95% CI) versus integration range $R = -L = \lambda l$, compared with the bulk-phase pressure differences $P_{\rm R}^{\rm i} - P_{\rm L}^{\rm i}$ (dashed blue line).

5. Conclusion. This study demonstrates mechanical equilibrium in underdamped active matter by integrating robotic experiments with a theoretical framework. Our measurements quantitatively confirm that the intrinsic pressure difference across the activity interface is balanced by the emerged polarization force, providing the first experimental verification of the $P^{\rm i}$ framework. Furthermore, the real-time control and parameter adaptability of our robotic system provide a novel platform suited for both probing force balance conditions and exploring broader phenomena in active matter, such as collective dynamics in multi-agent systems and adaptive behaviors in complex environments.

Acknowledgments. This work was supported by the National Natural Science Foundation of China (Grant Nos. T2325027, 12274448, T2350007, 12404239, 12174041, 12325405, 12090054, and T2221001), and the National Key R&D Program of China (Grant No. 2022YFF0503504).

References

[1] Ramaswamy S 2010 *Annu. Rev. Condens. Matter Phys.* **1** 323
[2] Marchetti M C, Joanny J F, Ramaswamy S, Liverpool T B, Prost J, Rao M, and Simha R A 2013 *Rev. Mod. Phys.* **85** 1143
[3] Bechinger C, Di Leonardo R, Löwen H, Reichhardt C, Volpe G, and Volpe G 2016 *Rev. Mod. Phys.* **88** 045006
[4] Tailleur J and Cates M E 2008 *Phys. Rev. Lett.* **100** 218103
[5] Fily Y and Marchetti M C 2012 *Phys. Rev. Lett.* **108** 235702
[6] Buttinoni I, Bialké J, Kümmel F, Löwen H, Bechinger C, and Speck T 2013 *Phys. Rev. Lett.* **110** 238301
[7] Redner G S, Hagan M F, and Baskaran A 2013 *Biophys. J.* **104** 640a
[8] Cates M E and Tailleur J 2015 *Annu. Rev. Condens. Matter Phys.* **6** 219
[9] Vicsek T, Czirók A, Ben-Jacob E, Cohen I, and Shochet O 1995 *Phys. Rev. Lett.* **75** 1226
[10] Vicsek T and Zafeiris A 2012 *Phys. Rep.* **517** 71
[11] Bricard A, Caussin J B, Desreumaux N, Dauchot O, and Bartolo D 2013 *Nature* **503** 95
[12] Liu S, Shankar S, Marchetti M C, and Wu Y 2021 *Nature* **590** 80

[13] Yang Q, Liang H, Liu R, Chen K, Ye F, and Yang M 2021 *Chin. Phys. Lett.* **38** 128701
[14] Baconnier P, Shohat D, López C H, Coulais C, Démery V, Düring G, and Dauchot O 2022 *Nat. Phys.* **18** 1234
[15] Liu R, Gong J, Yang M, and Chen K 2023 *Chin. Phys. Lett.* **40** 126402
[16] Takatori S C and Brady J F 2015 *Phys. Rev. E* **91** 032117
[17] Epstein J M, Klymko K, and Mandadapu K K 2019 *J. Chem. Phys.* **150** 164111
[18] Gompper G, Winkler R G, Speck T *et al.* 2020 *J. Phys.: Condens. Matter* **32** 193001
[19] Takatori S C, Yan W, and Brady J F 2014 *Phys. Rev. Lett.* **113** 028103
[20] Solon A P, Stenhammar J, Wittkowski R, Kardar M, Kafri Y, Cates M E, and Tailleur J 2015 *Phys. Rev. Lett.* **114** 198301
[21] Paul S, Jayaram A, Narinder N, Speck T, and Bechinger C 2022 *Phys. Rev. Lett.* **129** 058001
[22] Pellicciotta N, Paoluzzi M, Buonomo D, Frangipane G, Angelani L, and Di Leonardo R 2023 *Nat. Commun.* **14** 4191
[23] Solon A P, Fily Y, Baskaran A, Cates M E, Kafri Y, Kardar M, and Tailleur J 2015 *Nat. Phys.* **11** 673
[24] Ginot F, Theurkauff I, Levis D, Ybert C, Bocquet L, Berthier L, and Cottin-Bizonne C 2015 *Phys. Rev. X* **5** 011004
[25] Takatori S C, De Dier R, Vermant J, and Brady J F 2016 *Nat. Commun.* **7** 10694
[26] Ginot F, Solon A, Kafri Y, Ybert C, Tailleur J, and Cottin-Bizonne C 2018 *New J. Phys.* **20** 115001
[27] Xie K, Gorin B, Cerbus R T, Alvarez L, Rampnoux J M, and Kellay H 2022 *Phys. Rev. Lett.* **129** 138001
[28] Wysocki A, Elgeti J, and Gompper G 2015 *Phys. Rev. E* **91** 050302
[29] Fily Y, Kafri Y, Solon A P, Tailleur J, and Turner A 2017 *J. Phys. A: Math. Theor.* **51** 044003
[30] Junot G, Briand G, Ledesma-Alonso R, and Dauchot O 2017 *Phys. Rev. Lett.* **119** 028002
[31] Liu P, Li L, Ning L, Zheng N, and Yang M 2023 *J. Phys.: Condens. Matter* **35** 445102
[32] Wysocki A, Dasanna A K, and Rieger H 2022 *New J. Phys.* **24** 093013
[33] Sun Z, Li L, Wang C, Wang J, Chen H, Wang G, Liu L, Ye F, and Yang M 2025 arXiv:2507.14644 [cond-mat.soft]
[34] Speck T and Jack R L 2016 *Phys. Rev. E* **93** 062605
[35] Omar A K, Wang Z G, and Brady J F 2020 *Phys. Rev. E* **101** 012604
[36] Li L, Sun Z, and Yang M 2025 *Proc. Natl. Acad. Sci. USA* **122** e2505010122
[37] Herrera P and Sandoval M 2021 *Phys. Rev. E* **103** 012601
[38] Arlt J, Martinez V A, Dawson A, Pilizota T, and Poon W C 2019 *Nat. Commun.* **10** 2321
[39] Row H and Brady J F 2020 *Phys. Rev. E* **101** 062604
[40] Söker N A, Auschra S, Holubec V, Kroy K, and Cichos F 2021 *Phys. Rev. Lett.* **126** 228001